iScience

CellPress
OPEN ACCESS

Article

Highly sensitive and extremely durable wearable e-textiles of graphene/carbon nanotube hybrid for cardiorespiratory monitoring

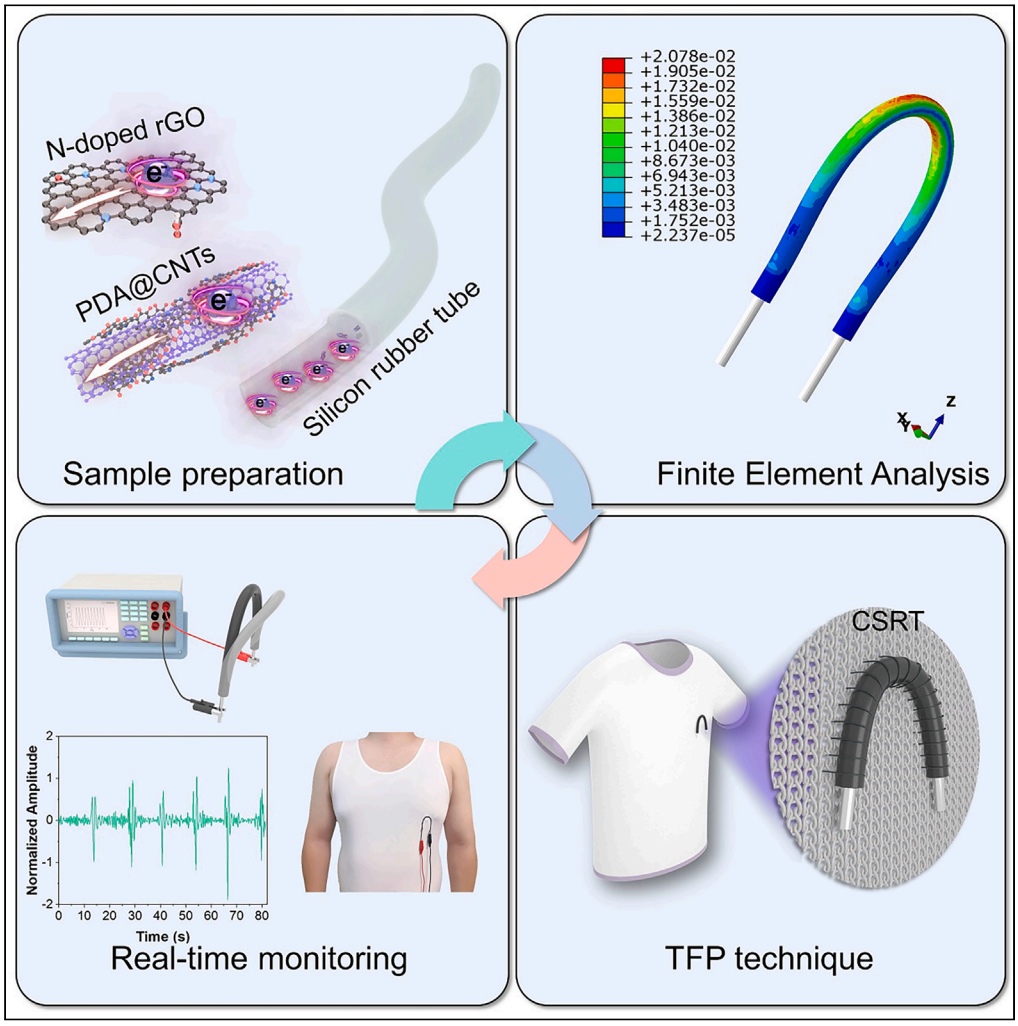

Sirui Tan, Shaila Afroj, Daiqi Li, ..., Guangming Cai, Nazmul Karim, Zhong Zhao

shaila.afroj@uwe.ac.uk (S.A.)
nazmul.karim@uwe.ac.uk (N.K.)
zzhao@wtu.edu.cn (Z.Z.)

Highlights

N-doped rGO and polydopamine coated CNT (rGO/CNT) hybrid was prepared

Conductive silicon rubber tube (CSRT) was prepared via vacuum filling of rGO/CNT

CSRT was highly sensitive, flexible, and extremely durable

CSRT was embroidered into a vest to sense wearer heart and breathing rate

Tan et al., iScience 26, 106403
April 21, 2023
https://doi.org/10.1016/j.isci.2023.106403

iScience

CellPress
OPEN ACCESS

Article

Highly sensitive and extremely durable wearable e-textiles of graphene/carbon nanotube hybrid for cardiorespiratory monitoring

Sirui Tan,[1,2] Shaila Afroj,[3,*] Daiqi Li,[1,2] Md Rashedul Islam,[3] Jihong Wu,[1,2] Guangming Cai,[1,2] Nazmul Karim,[3,*] and Zhong Zhao[1,2,4,*]

SUMMARY

Electroconductive textile yarns are of particular interest for their use as flexible and wearable sensors without compromising the properties and comfort of usual textiles. However, the detection of fine actions of the human body is quite challenging since it requires both the relatively higher sensitivity and stability of the sensor. Herein, highly sensitive, ultra-stable, and extremely durable piezoresistive wearable sensors were prepared by loading N-doped rGO and polydopamine-coated carbon nanotubes into silicon rubber tube. The wearable sensors thus produced show an excellent ability to sense subtle movement or stimuli with good sensitivity and repeatability. Furthermore, by bending the straight conductive silicon rubber tube (CSRT) into three different patterns, its sensitivity was then dramatically increased. Finally, the CSRT was found capable of sensing cardiorespiratory signals, indicating that the sensor would be an important step toward realizing bio-signal sensing for next-generation personalized health care applications.

INTRODUCTION

Wearable electronic textiles (e-textiles) are of great interest for personalized healthcare applications[1–3] as they are flexible, comfortable, and lightweight as well as maintaining the desirable electrical property.[4,5] In recent years, wearable sensors integrated into clothing have widely been investigated as reliable platforms for monitoring biomedical,[6] physiological,[7] and biomimetic[8] signals. Several e-textile platforms were reported to capture and monitor physiological signals from the human body,[9] including body temperature,[10] oxygen saturation level,[11] heart rate,[12] and human body motion.[2,13] Both yarn and fabric-based sensors have been employed to produce such wearable e-textile sensors.[14–17] Despite that the amount and position of conductive materials in the whole configuration vary from one study to another, the performances of e-textile sensors mainly depend on the electrical conductivity of nano-micro materials deposited on textiles, and the flexibility of textile substrates.[18,19]

Carbonaceous materials such as graphene and carbon nanotubes (CNT) have widely been used as electrically conductive materials for e-textiles applications,[20] due to their advantages including excellent electrical conductivity,[21–23] good mechanical properties[24–26] and high specific surface area.[27,28] However, the performances of e-textile sensors based on carbonaceous materials can easily be influenced by external stimuli such as the room temperature,[29] oxidation,[30] corrosion,[31] abrasion[32] and washing[33] of conductive materials. Researchers have developed various methods to overcome such limitations. For instance, Kim et al. prepared boron-coated multi-walled CNT which maintains superior conductivity even at 1000 °C.[34] Joh et al. used PET and PDMS layers to cover conductive materials to prevent the effect of water and oxygen.[35] Zhou et al. bridged CNT to PDMS with a silane coupling agent (KH550) to realize the stable adhesion of conductive materials to the substrate.[36] However, there remain several challenges that need to be addressed to produce robust and reliable wearable e-textiles. The conductivity and durability of graphene-based materials need further improvements to enable the detection of fine actions of the human body.[37] Additionally, the fatigue of the sensor caused by the abrasion during its long-term service is a great concern for such e-textiles.[38] Furthermore, the polymer coatings lead to an increase in the thickness, which adversely affects the mechanical properties of the sensor, such as flexibility, elasticity, and recoverability.[39]

[1]State Key Laboratory of New Textile Materials and Advanced Processing Technologies, Wuhan Textile University, Wuhan 430073, China

[2]School of Textile Science and Engineering, Wuhan Textile University, Wuhan 430200, China

[3]Centre for Print Research (CFPR), University of the West of England, Frenchay, Bristol BS16 1QY, UK

[4]Lead contact

*Correspondence: shaila.afroj@uwe.ac.uk (S.A.), nazmul.karim@uwe.ac.uk (N.K.), zzhao@wtu.edu.cn (Z.Z.)

https://doi.org/10.1016/j.isci.2023.106403

The doping of graphene structure with nitrogen atoms has been proven to be a feasible method to improve its conductivity.[40] The blending of graphene sheets with CNT is another way to realize improved conductivity, as CNT can bridge graphene sheets to promote electron migrations.[41] However, the poor binding strength between substrate materials and carbon-based materials leads to poor washability, durability, and occurrence of hysteresis.[42] Filling carbonaceous nanomaterials into the matrices is a feasible way to fabricate continuous fibers or filaments with satisfied conductivity. For instance, carbon-based nanofillers can be integrated into polyethylene matrices via coaxial electrospinning to fabricate thermal conductive nanofibers.[43] Besides, rGO and MXene can be injected into polypropylene tubes to shape these nanocarbon materials into fiber-like carbonaceous hybrids for potential wearable supercapacitor applications.[44] Silicon rubber could be a potential solution as a substrate to mix or cover the conductive materials to form the e-textile due to their good stretchability, flexibility[45,46] and elastic recovery.[47] Meanwhile, the hollow tube can act as a mold to model the nanocarbon fillers in a continuous shape. These advantages ensure good mechanical performances of wearable sensors as well as protecting the continuous conductive materials from abrasion, oxidation, and water.[48] In addition, from the perspective of commercial application, the durability of the sensor can be dramatically improved, thus, the use cost of this sensor can also be lowered. Moreover, using the silicon rubber as the container to cover the conductive powder has more advantages over the mixing method due to the fact that mixing the conductive powder with the silicon rubber directly would have an adverse effect on the mechanical properties of the final e-textile, and the sensitivity of the e-textile can be tailored by adjusting the quantity and compression degree of the conductive powder. Meanwhile, the conductive powder filled inside the matrix can support the outer layer of the matrix and reduce its deformation extent, thus, balancing deformation with recovery and enhancing the reproducibility and stability of the sensor. Compared with liquid-phase and paste-like filling materials, the solid-state conductive powder has higher rigidity. By filling these solid substances into the matrix, the hysteresis effect can be weakened as the extent of deformation can be further reduced.

In this study, N-doped rGO and PDA-coated CNT (PDA@CNT) were separately prepared and then blended together to form a mixed powder with enhanced conductivity. The PDA layer formed on CNTs enhances the adhesion between CNT and graphene sheets and improves the stability of the mixture. The rGO/PDA@CNT hybrid powder was then covered by silicon rubber and mixed with Ecoflex to fabricate flexible e-textile sensors. Doping nitrogen sources can improve the conductivity of hybrid carbon materials-based wearable e-textiles, while the silicon substrates protect them from abrasion, ensuring prolonged service life of the wearable sensors. The as-prepared conductive silicon rubber tube (CSRT) was mounted on the elastic Lycra vest via a tailored fiber placement (TFP) embroidery technique. It provides good firmness and realizes the fixation of filaments at desired positions with variable structures. The sensor was then able to monitor the wearer's signals of respiration and heart rate.

RESULTS AND DISCUSSION

Characterization

CNT has an average radius of approximately 50 nm (Figure 1B). It can be observed from the combined mapping results (Figure 1C) that nitrogen atoms are evenly scattered on the CNT surface after the coating process, indicating successful self-polymerization of dopamine on CNTs. This is consistent with the appearance of a nitrogen peak at ~400 eV in the overall XPS spectrum (Figure 1G) of the mixed powder. By further comparing the obtained and the peaks reported in the literature, the peaks at the binding energy of ~400.4 and ~398.4 eV (Figure 1H) can be assigned to the pyrrolic N and pyridinic N,[49] respectively. Similarly, the peaks at the 2θ of 26.0° and 42.6° (Figure 1I) can be assigned to (002) and (100) planes of CNTs,[50,51] respectively. The results from XPS and XRD jointly indicate the existence of PDA coverage on CNTs. However, no obvious trace of N-doped rGO can be observed from the SEM image of the mixed powder (inset in Figure 1I) as the content ratio of N-doped rGO in the filling material is relatively low. This is also reflected by the fact that no prominent diffraction peaks of amorphous graphene were observed in the XRD spectrum of filling materials (Figure 1I).

Sensing capability/electro-mechanical characterization of CSRT and CEF filaments

To assess the sensing capability, CSRT (1.14 S/m) and conductive Ecoflex filament, CEF (0.24 S/m) filaments were subjected to a single compression test (Figures 2A–2F). The changes in the resistance of filaments were measured and recorded via the NI-9219 data acquisition card (National instrument, USA). Linear correlations between the resistance of the CSRT as well as CEF and the compression force applied to the sensors can be clearly observed (Figure 2A and 2D). It is notable that an open circuit occurs for CEF when the

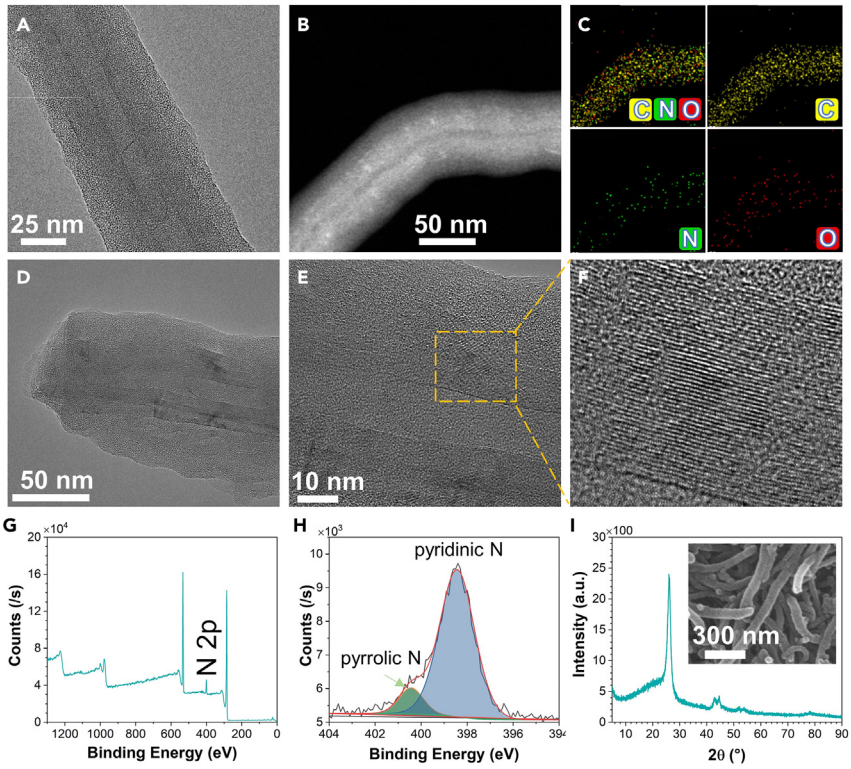

Figure 1. Characterization results of CSRT

(A) TEM image of the PDA@CNT.

(B) HAADF image of CSRT.

(C) Mapping results of CSRT.

(D) TEM image of CSRT.

(E and F) CNTs in the CSRT.

(G) Wide scan XPS spectrum.

(H) high-resolution spectrum of N1s.

(I) XRD spectrum and SEM (inset) of the mixed powder of PDA@CNT and N-doped rGO.

compression force reaches 38.2 N (Figures 2D and 2E). The open circuit can be attributed to the structural difference between the two filaments (Figure 2D). When the compression force is applied to those two filaments, CEF would become a totally flat two-dimensional structure due to the lower rigidity and softer texture. However, the filling conductive powder inside CSRT will be more tightly compressed while its three-dimensional structure still remains. Specifically, a breakpoint inside the CEF may occur when the force is applied to the filament, leading to the compression of filling materials inside it and sliding of particles against the stress point. Therefore, a clear negative correlation between the resistance of CSRT and the applied compression force can be observed, while the correlation turned positive in the case of CEF.

As presented in Figure S4A, the compression strain curves as the function of force overlap well when the force increased stepwise from 10 to 40 N, indicating stable responsiveness of CSRT to dynamic compression load. However, distinct steps can be observed in the compression strain curves of CEF when the force increased at the intervals of 10 N, suggesting that the CEF deformed and rebounded at different speeds and to different extents when the force changed stepwise. Moreover, wider gaps between the compression and compression back sections can be observed in the compression curves of CEF, reflecting severe hysteresis that CEF exhibited during its compression-recovery cycles. The compressive deformation of CSRT includes the deformation of the silicon rubber tube and the compression of the conductive powder inside. However, as the CEF is made from the Ecoflex blended with the sparsely dispersed conductive nanoparticles which barely affect the strength of the matrix, its deformation and recovery depend mainly on the flexibility of the matrix itself. When the same compression load is applied, the compression strain of CSRT is smaller than CEF as the solid conductive powder inside the CSRT can support the rubber matrix

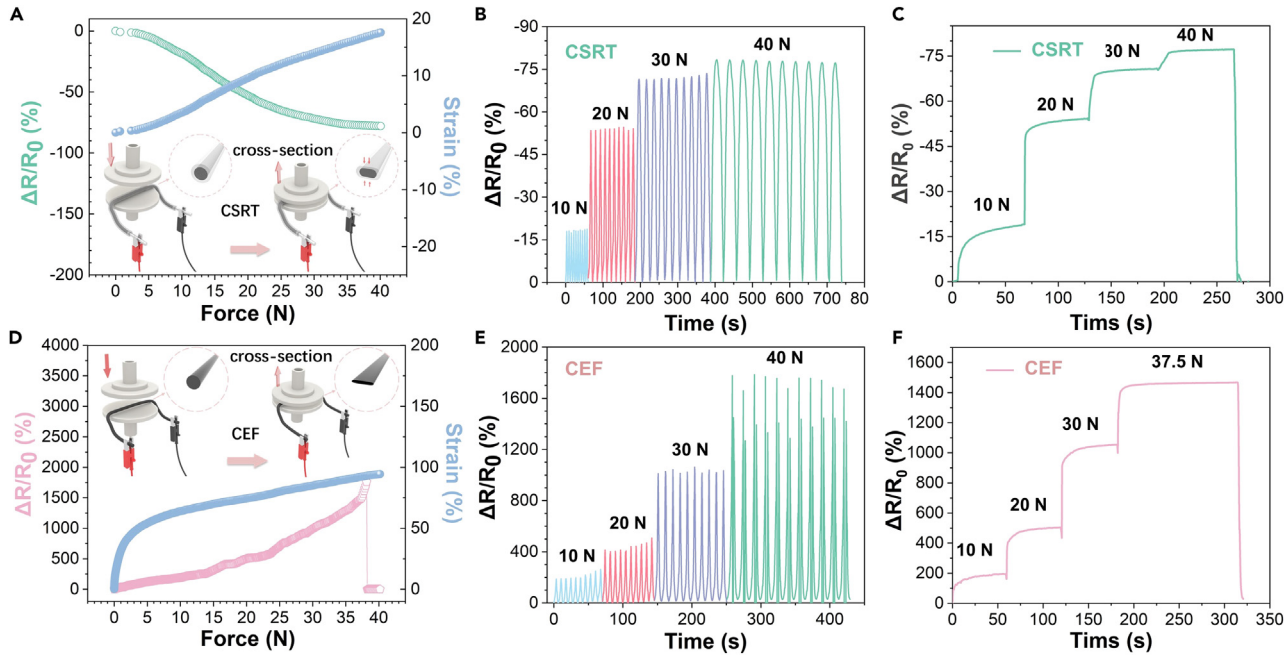

Figure 2. Electro-mechanical test results of CSRT and CEF filaments

(A) A single compression test result of CSRT filament from 0 to 40 N.

(B) A stepped compression cyclic test result of CSRT.

(C) A stepped quasi-static test result of CSRT filament.

(D) A single compression test result of CEF filament from 0 to 40 N.

(E) A stepped compression cyclic test result of CEF.

(F) A stepped quasi-static test result of CEF filament.

against further compression. When the compression load is removed, the CSRT can rapidly recover to its original shape due to its lower compression strain. This narrows the hysteresis caused by the unsynchronized deformation and recovery speed.

Table S1 shows the comparison of the CSRT and CEF with the previous studies. The CSRT and CEF filament present a larger working range than that reported in the previous studies,[52–59] which is significantly higher than general wearable pressure.[60] Additionally, they indicate a relatively higher sensitivity as a conductive yarn compared to previous studies.[52–58,61,62] Moreover, the signal output of the CSRT filament was stable and repeatable, and its flexibility and bendability demonstrate its excellent capability as a wearable filament.

Figures 2B and 2E show the stepped cyclic test results for the CSRT and CEF. The compression force was increased from 10N to 40N with the same compression speed employed in the single test. During the cyclic test, CSRT presented excellent durability and stability, and the resistance of CSRT was not changed significantly before and after the test. It can be seen from Figures 2B and 2E that the deformation speed of CEF is faster than that of CSRT. Due to the relatively lower rigidity and recovery speed, the cyclic result of CEF is unstable, especially when the load is around 38.2 N. The changes in resistance of CEF suddenly increased from 1300% to 1600-1800%, and then an open circuit occurred. However, the open circuit happened whenever the compression force reached ~38.2 N during the cyclic test, which means that it can be used as an open circuit alarm.

Figures 2C and 2F exhibit quasi-static test results of those two filaments. The tensile machine will keep the compression load for 1 min at 10N, 20N, 30N, and 40N for CSRT, and at 10N, 20N, 30N, and 37.5N for CEF. Both filaments demonstrate good stability during this test, especially when the compression force is over 20N. However, when the compression is lower than 20N, it takes more than 10 s for their resistance to become stable.

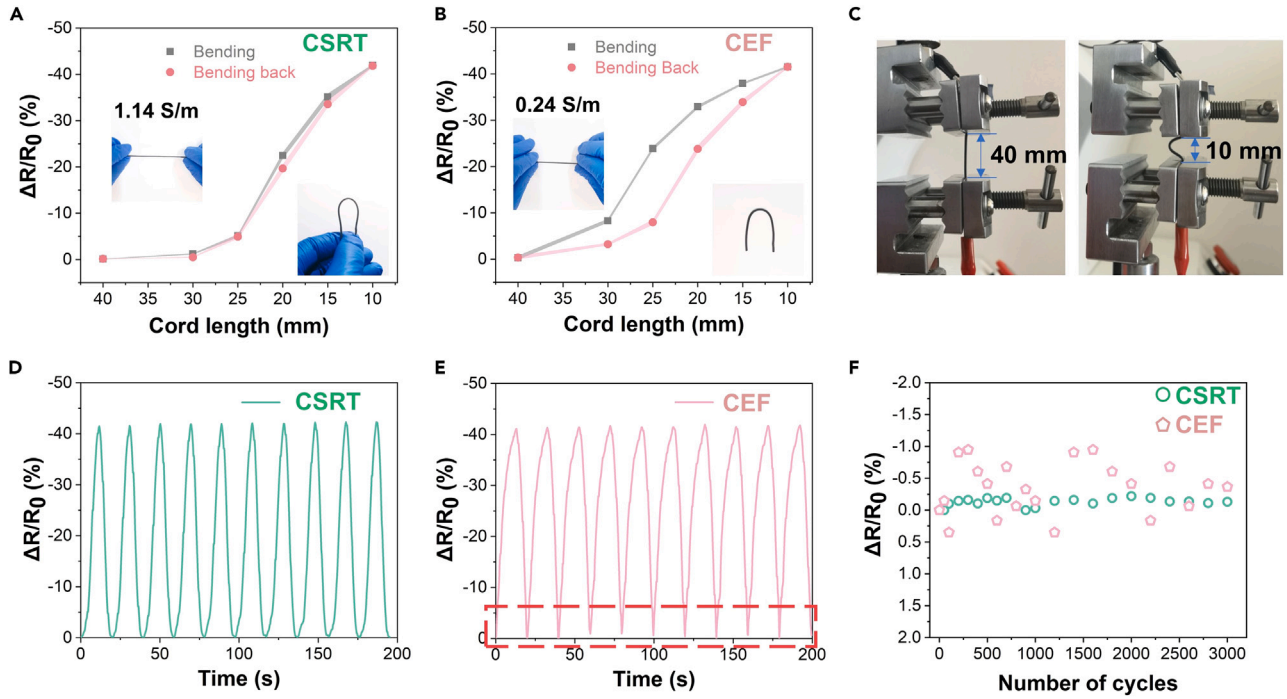

Figure 3. Bending test result of CSRT and CEF filaments

(A) Bending and bending back result of CSRT filament with error band.

(B) Bending and bending back result of CEF filament with error band.

(C) Optical image of the CSRT filament during the bending test.

(D) Bending cyclic test result of CSRT filament.

(E) Bending cyclic test result of CEF filament.

(F) 3000 times cyclic test result of CEF and CSRT filament.

Performance and flexibility of CSRT and CEF filaments

The flexibility of the as-prepared graphene-CNT-based CSRT and CEF filaments was further investigated. Figures 3A and 3B show the changes in resistances per total length of CSRT and CEF filaments at various bending positions with concave down at various cord lengths (Figure 3C). The cord lengths were controlled with the tensile tester. Here, the cord length is defined as the distance between the tensile tester grips for the filament material under investigation.[63,64] As seen in Figure 3A, a repeatable response in forward (bending) and reverse (bending back) directions was observed. Similarly, for the CEF, the change in resistance was repeatable in both the forward (bending) and reverse (bending back) directions (Figure 3B).

When Figure 3A and 3B are compared, the error band of the CSRT is relatively smaller than that of CEF, especially at the beginning of the bending process. Moreover, the hysteresis gap between bending and bending back is narrowed when the conductive powder was filled into the silicon rubber tube (Figure 3A). These results indicate that the CSRT has better repeatability and stability. Unlike the compression test, where the change in resistance of CEF increased with the increase of the load, a negative correlation between the resistance of the CEF and its cord length for bending was observed. This may be due to the lower rigidity of the Ecoflex exhibited during the bending test. More specifically, Ecoflex is soft and easy to be bended; hence there is no significant change in the radius of cross-section and volume at the bending point, while the conductive powder inside the CEF was compressed and became closer, facilitating the current flow, which would lead to the decrease in the resistance of the CEF.

After this, 10 cycles and 3000 cycles of bending cyclic tests were carried out for both filaments (Figures 3D–3F). This can be observed in Figures 3A and 3D, the resistance of the CSRT changed slightly at the beginning of the bending process, and the resistance of it decreased significantly from 30 to 10 mm, especially 25-15 mm. It can be also found that compared to CSRT, the CEF's $\Delta R/R_0$ reversed much quickly at the lowest points (also points of 40-mm cord length) as the curves of CEF is non-differentiable at these lowest points of $\Delta R/R_0$ (Figure 3E). From

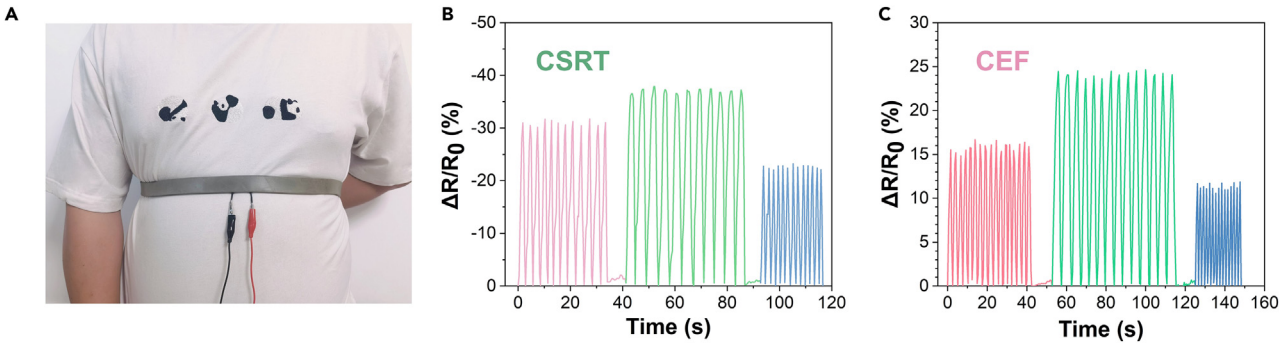

Figure 4. Respiratory signal sensing of the CSRT and CEF sensors

(A) Image of the subject placed the sensor under the elastic band on the below chest location.

(B) Resistance of CSRT variation due to respiration.

(C) Resistance of CEF variation due to respiration.

the perspective of integration, this non-differentiable nature of the CEF's lowest $\Delta R/R_0$ points means that the CEF exhibited higher sensitivity (higher absolute value of $\Delta R/R_0$ compared to CSRT) at the beginning of the bending process. However, it exhibited lower sensitivity at the end of the bending process as the absolute value of CEF's $\Delta R/R_0$ increased at a slightly lower speed than that of CSRT.

Figure 3F is the 3000 cycles bending cyclic test results of the two filaments, the changes in resistance were recorded whenever the cord length reaches 40 mm (straight filament). It can be clearly seen that the resistance of the CSRT is more stable during the long-term cyclic test ($\Delta R/R_0$ is around 0.02% to −0.15%), while that of CEF is scattered ($\Delta R/R_0$ is around 0.34% to −0.94%).

Furthermore, a series of joints activities monitoring tests were carried out to investigate the bendability, reliability, and capability of the CSRT and CEF to monitor human activities. The experimental produces along with corresponding results (presented in Figure S7) and the discussion of the tests are placed in Supporting Information.

Respiration monitoring capability of CSRT and CEF filaments

To investigate the bio-signal sensing performance of those two filaments for real-life implications, they were further tested as breathing sensor. They were placed under an elastic band (Figure 4A) around the chest location. The NI-9219 data acquisition card was connected with filaments to record the changes in the resistance during the breathing test. The breathing test started with normal breath; the subject stopped breathing for a few seconds after 10–12 breathes, and then continued to breathe deeply. After 10–12 deep breathes, the subject started a fast-breathing and the responses of those two filaments to the fast breathing were recorded (as shown in Figures 4B and 4C). During the three-step breathing test, both sensors performed well with excellent stability and outstanding response speed during the fast-breathing test. Although, the changes in resistance fluctuate a little bit during the test, which may be due to not being able to maintain the same breath range by the subject during the test. Nevertheless, such results can still demonstrate that the conductive sensors are capable of bio-signal sensing.

During all the tests above, the CSRT represents a relatively much better performance as a sensor, as it shows relatively more stable signal output, fast recovery speed, and higher sensitivity during the compression and bending test. As for the CEF, it exhibits a good elasticity and relatively greater changes in resistance during the tests, however, the strength and recovery speed of the CEF were significantly weakened due to added PDA@CNT and N-doped graphene powder. Also, the quantity of the conductive powder has a great influence on not only the mechanical properties of CEF but also the electro-mechanical properties. Although it shows a relatively unstable signal output, it presents a stable break circuit when the load arrives at a specific value during the cyclic tests, which exhibits its capability as an open-circuit alarm material.

Comparison of the CSRT structures

It is worth mentioning that we observed lower sensitivity and unstable signal output when the compression load was maintained at lower level. This unstable performance might be caused by gaps in the conductive

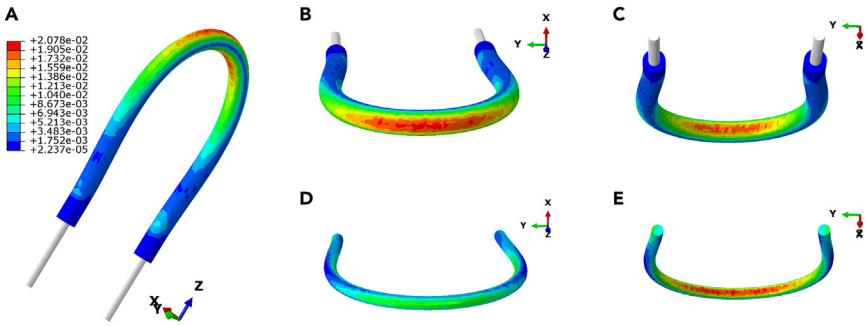

Figure 5. Simulation of the effect of bending on the strain of the CSRT obtained in ABAQUS

(A) Strain distribution of the bended CSRT. Strain distribution on the (B) outer surface and (C) inner surface of the bended CSRT. Strain distribution on the (D) outer surface and (E) inner surface of the conductive powder unit within the bended CSRT.

powder, the CSRT displays an insensitive response to the pressure applied as the conductive powder was first compressed. Once the force applied exceeds this insensitive range, the CSRT exhibits a sharp response to the force as its electrical resistance changes rapidly since the gaps have disappeared. Therefore, to eliminate this insensitive working range in real-life application, the CSRT was bended into three different shapes to fully compress the conductive powder loaded in it.

To reveal the impact of bending force within the CSRT, the process of bending the CSRT into a "U" shape was simulated in ABAQUS. As Figure 5A shows, bending the CSRT into the "U" shape caused the increase of strain within the arch section of the bended CSRT sample. More specifically, the outer and inner surfaces of the bended CSRT underwent obvious stretch (Figure 5B) and compress (Figure 5C), respectively. As the gaps between the tubes and the stainless rods were sealed by Ecoflex, the conductive powder inside the tube cannot overflow alongside the axis direction of the tube. When the CSRT was bended, the inner surface of the conductive powder was densely compressed (Figure 5E) due to the force applied by the tube. It is also notable that the strain of the outer surface of the conductive powder section (Figure 5D) was not dramatically increased to the extent of that observed from the surface of the tube (Figure 5B). The possible reason is that the top area of the conductive powder unit turns relatively sparser when it is shaped into a "U" pattern during the bending of the CSRT. Overall, the simulation results confirm that the bending action provided the pre-load for the CSRT.

However, when more bending arcs are formed, the rigidity of the CSRT will become higher, and the recovery speed will become lower which might lead to an unstable resistance curve during the tests. Therefore, three structures (P1, P2, and P3) were designed and manufactured by TFP (Figure 6A), which were tested under the same condition as the straight CSRT.

Figure 6B illustrates the single compression test results of three structures. Figure 6B shows that all three structures, particularly P3, can improve the sensitivity significantly, when the compression load is under 10N. However, when the force exceeds 10N, the changes in resistance of P3 are not apparent (resistance changes from 60% at 10N to 70% at 40N). It may be due to two arcs push the conductive powders from two sides to the middle area of the structure which can provide higher pre-loads than the other two structures.

Figures 6C–6E indicate the stepped cyclic test results of the three structures, and Figures 6F–6H summarize the stepped long-term stability test results of those three structures. Compared to the straight CSRT, the sensitivity of the three structures from 0 to 5N, increased from 0.01 N^{-1} to 0.052 N^{-1},0.09 N^{-1}, and 0.048 N^{-1}. Compared to P2 and P3, P1 shows relatively higher stability and repeatability. There was not a significant drift during both the cyclic test and long-term stability test of structure 1. Moreover, there is a clear difference in the resistance of structure 1 between each load step.

In contrast, the changes in resistance of P2 and P3 fluctuated during the cyclic tests. Although the resistance of P2 did not present an evident drift during the stepped long-term stability tests like P3, the resistance of

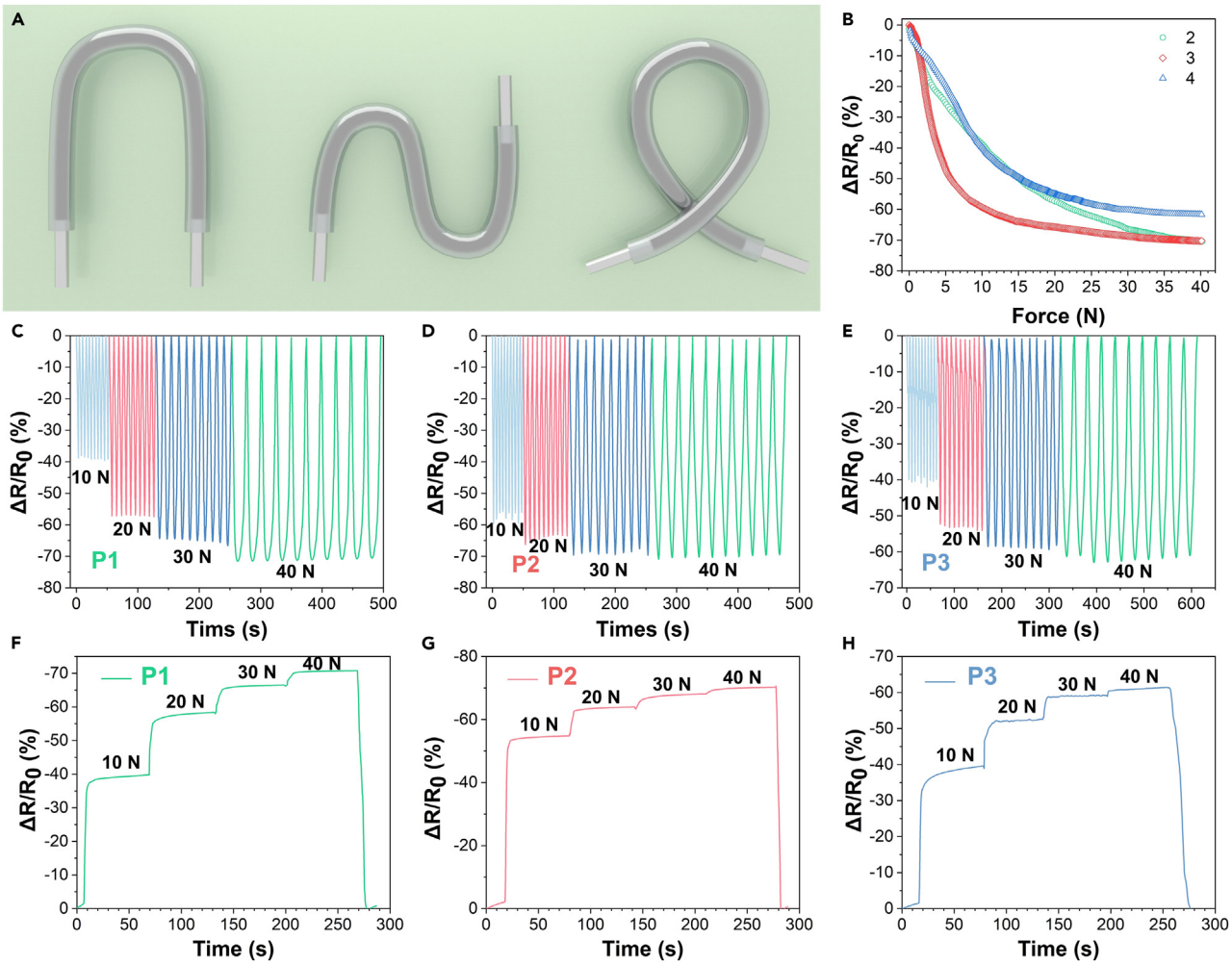

Figure 6. Electro-mechanical test results of the three different structures

(A) CSRT in three different structures.

(B) Single compression test results of the three structures from 0 to 40N.

(C–E) Stepped cyclic test results of the three structures, respectively.

(F–H) Stepped quasi-static test results of the three structures, respectively.

P2 did not describe a clear difference when the compression load reached 30N and 40N. Figure 6D shows that the changes in resistance of P2 at 30N and 40N loads were almost the same, which might have a significant influence on the final applications.

Compared to P2 and P3, P1 exhibits excellent stability of signal output and a more linear resistance-to-force correlation. Moreover, P1 shows a significantly higher sensitivity compared to straight CSRT while the load is under 10 N. Although, P2 presents a relatively most heightened sensitivity at lower compression force, its durability and stability are lower than P1. As discussed above, the resistance of P2 did not exhibit a clear difference when the load reached 30N and 40N.

Respiratory and pulse signal sensing

In order to investigate the bio-sensing capability of the P1 sensor, it was used to detect and measure the pulse and cardiac signals in addition to the breathing test. Figure 7A shows the changes in resistance of P1 during the respiration process. Similar to the straight CSRT, it offers good capability of detecting breathing signals and the collected respiration data was stable without observing any noise.

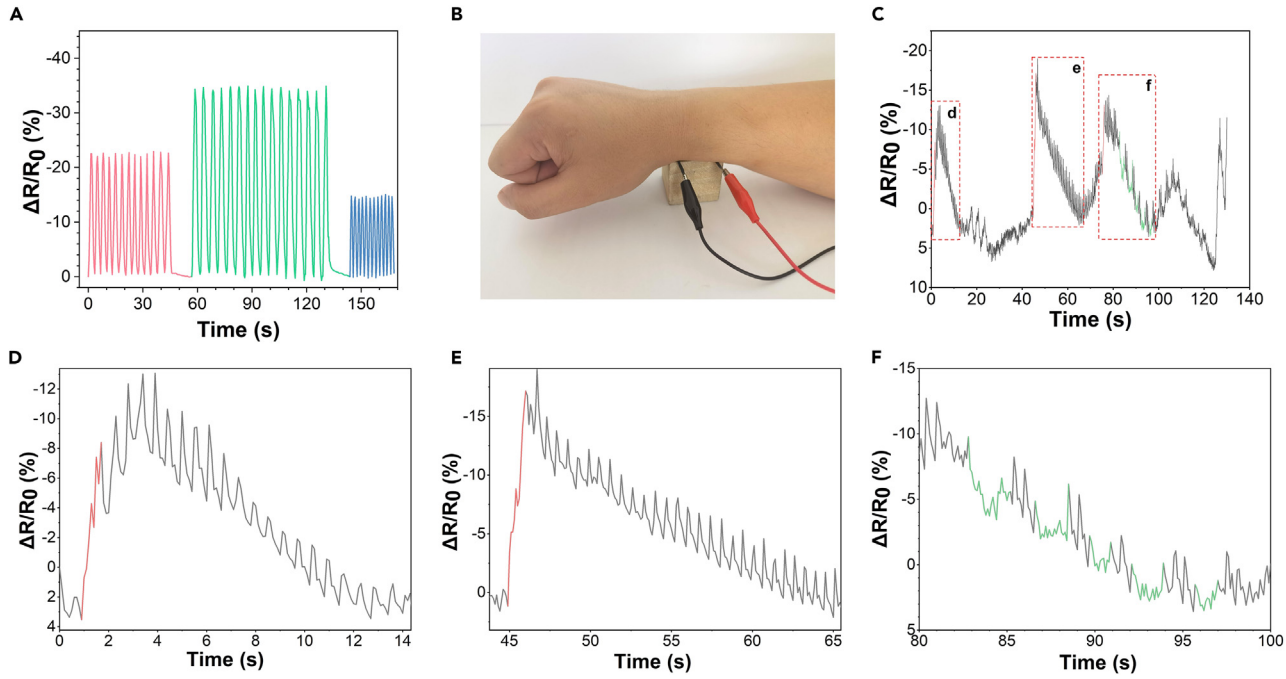

Figure 7. Respiratory and pulse signal captured by P1

(A) Respiratory signal captured by P1.

(B) Image of the sensor under the wrist during the pulse signal measuring.

(C) Pulse signal captured by P1.

(D) Expanded version of (c) from 0 s to 14 s.

(E) Expanded version of (c) from 45 s to 65 s.

(F) Expanded version of (c) from 80 s to 100 s.

The sensor was then placed between the right part of the wrist and a wooden cube as shown in Figure 7B (Video S1). Figures 7D–7F show the change in resistance due to the wrist pulse for a selected section of total 2 min pulse recorded. During the test, it was found that whenever the subject breathed, the changes in resistance of the sensor increased suddenly (the red line in Figures 7D–7F), which may be due to the fact that the wrist was placed on the wooden cube. Therefore, every time the subject breathes, the wrist of the subject will apply a slight compression force on the sensor. To verify the data fluctuations were caused by the breath of subject, the subject breath 5 times quickly (the green waves in Figure 7F). It can clearly be seen that the sensor could capture both respiration signal and pulse signal. In addition, the pulse signals captured during the subject was holding his breath could be clearly observed. Although the trend of the resistance has a sharp drift due to the respiration, it still exhibits the high sensitivity of small bio-signal sensing. In order to eliminate the error caused by wrist movement during respiration, and to assess the sensors' capability of minor simulation/movement detection, the sensor was placed under an elastic band to measure the cardiorespiratory signals.

Cardiorespiratory signal sensing

To capture clean and integral bio-signals and eliminate noise/interferences, the sampling rate of the NI-9219 data acquisition card was set from 10 to 50 Hz. Additionally, a bandpass filter was applied to improve the reliability of the signal output of the sensor. The heartbeat rate varies from person to person, usually 60-100 times per min, namely 1 to 1.67 Hz. Considering the cardiac patients and athletes, the bandpass filter was set from 0.8 to 2 Hz for cardiac signal capturing. The cardiorespiratory test was carried out on two healthy male volunteers. During the cardiorespiratory test, Subject 1 breathed for around 3 min and then held his breath as long as he could (Video S2) while Subject 2 breathed every 10–15 s.

Figures 8A and 8B show the cardiorespiratory monitoring results of Subject 1 before and after filter. Figures 8F and 8G show the cardiorespiratory monitoring results of Subject 2 before and after filter. It

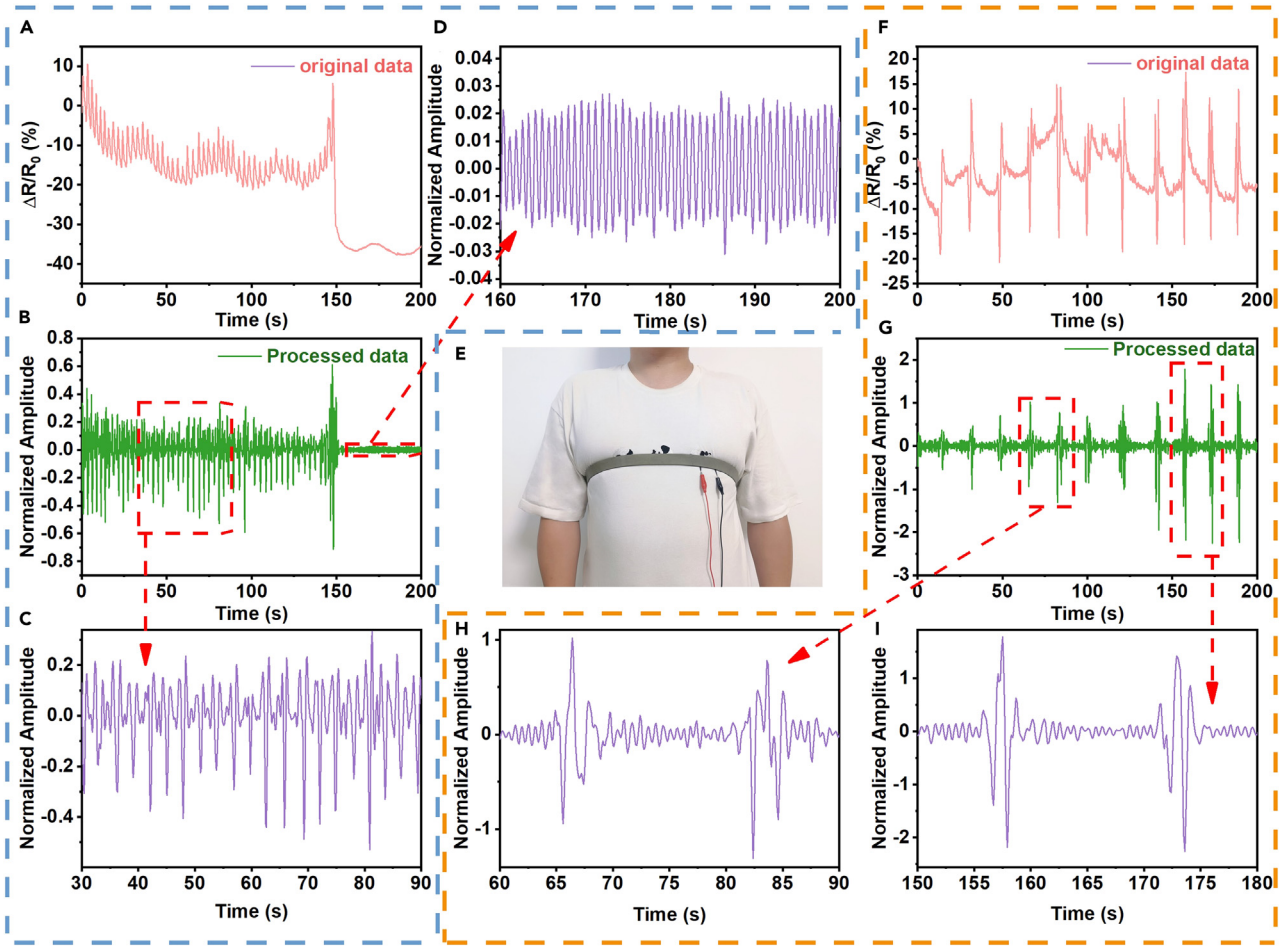

Figure 8. P1 cardiorespiratory signal sensing results

(A) Subject 1's cardiorespiratory signal captured by P1 without bandpass filter.

(B) Subject 1's cardiorespiratory signal captured by P1 with bandpass filter.

(C) Expanded version of (B) from 30 s to 90 s.

(D) Expanded version of (B) from 160 s to 200 s.

(E) Image of Subject 2 placed the P1 under the elastic band on the chest location.

(F) Subject 2's cardiorespiratory signal captured by P1 without bandpass filter.

(G) Subject 2's cardiorespiratory signal captured by P1 with bandpass filter.

(H) Expanded version of (G) from 60 s to 90 s.

(I) Expanded version of (G) from 150 s to 180 s.

shows that the bandpass filter helps to filter noises/interferences and makes both the cardiac signal and respiration signal more visible. Figures 8C and 8D show the change in resistance due to the cardiorespiratory for a selected section of Figure 8B. Figures 8H and 8I show the change in resistance due to the cardiorespiratory for a selected section of Figure 8F. Figure 8D exhibits a highly stable and clear cardiac signal captured by the sensors when the subject held his breath, which demonstrates the high sensitivity of the sensor. Figures 8H and 8I show that sensors can detect both cardiac and respiration signals at the same time. After each breath, the cardiac signals can clearly be monitored by the sensor. Even when the subject breathed normally (as shown in Figure 8C), the sensor is still capable of detecting cardiac signals clearly which shows the superior response speed and high sensitivity of the sensor. It can be clearly observed from Figures 8H and 8I that after each deep breath, the heart rate will decrease and then back to normal. It might be due to respiratory sinus arrhythmia, when the subject inhales and exhales, the heart rate will increase and decrease, respectively. Slight differences can be detected and measured by the sensor, which demonstrates higher accuracy and reliability of the sensor which provides the possibility of monitoring of patient's health at home.

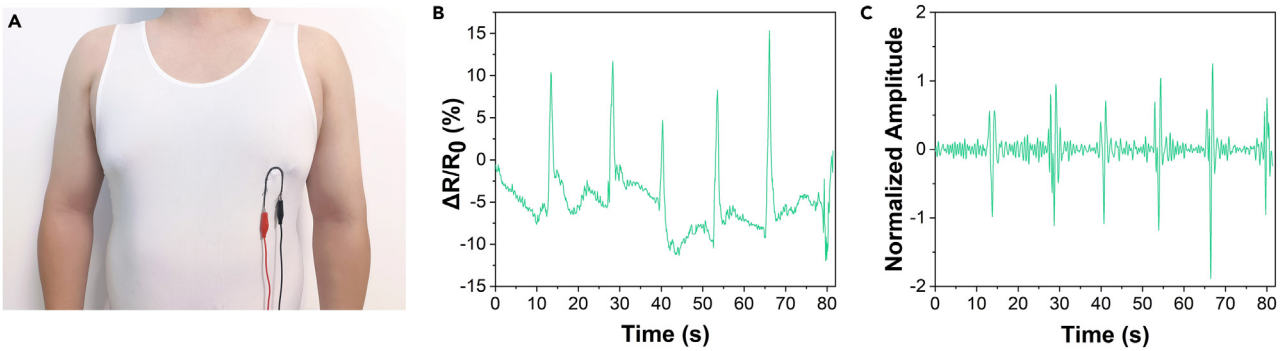

Figure 9. Cardiorespiratory signal captured by P1 on the Lycra vest

(A) Image of Subject 2 wearing the Lycra vest.

(B) Subject 2's cardiorespiratory signal captured by sensor without bandpass filter.

(C) Subject 2's cardiorespiratory signal captured by the sensor with bandpass filter.

Tightly fitting the sensor to the chest of the subject or improving the sensitivity of the sensor can improve the accuracy of cardiorespiratory signal monitoring. Although these two points can be easily realized by utilizing the elastic band, the pressure caused by tight binding may cause inconvenience and discomfort for the wearer.

To consider the capability of the CSRT for daily bio-signal monitoring without the elastic band, the CSRT sensor was sewed onto a vest via the tailored fiber placement (TFP) technique. The main advantage of the TFP is that the upper sewing thread and substrate fabric/cloth can also provide equivalent compression to the CSRT placed in between. Besides, as evidenced by the results of finite element analysis (Figure 5), when the CSRT was sewed onto the substrate in different bended shapes, more pre-loads to it can be generated to improve the sensitivity of the CSRT. Therefore, to investigate the capability of the sensor sensing the cardiac signal without the elastic band, the CSRT was fixed on a Lycra vest at the chest location by the tailored fiber placement technique (Figure 9A).

Same as the above test, the subject worn this Lycra vest and the resistance of the sensor was measured and record by the NI-9219 data acquisition card (Video S3), also the bandpass filter was used to reduce the noise during the cardiac signal-capturing process. Figures 9B and 9C show the test results before and after the filter. It can be clearly seen that, even without the help of the elastic band, the CSRT sensor can still capture the respiratory and cardiac signals. And the same situation can be clearly noticed in Figure 9C that when the subject exhaled, the heart rate decreased.

Figures 8 and 9 exhibit the capability of the CSRT sensor to capture the cardiorespiratory signal with and without the help of the elastic band. The experiments reveal that this CSRT sensor can capture clear cardiac signals while the subject was holding his breath, slow breathing, and normal breathing. Therefore, it is evident that this CSRT sensor has the capability to measure and monitor the cardiorespiratory signal as a wearable sensor. It is worth mentioning that the whole fabrication process of the CSRT took only 30 min for vacuum filling and further 30 min for the evaporation of water from the paste. The total time for the fabrication process can further be shortened with the use of the industrial vacuum instrument. Therefore, by ensuring the supply of adequate conductive paste and silicon rubber tubes, the CSRT can be manufactured continuously for large-scale industrial production. This manufacturing technique also features high reuse rate of the residual paste. The high durability and electro-mechanical performance of the CSRT thus ensures its potential commercial value.

Conclusion

In summary, two different conductive filament sensors were fabricated by using the N-doped rGO and PDA@CNT mixed powders (Figure 10). The CSRT exhibited excellent durability and sensitivity as well as lowered hysteresis during all the tests, while the CEF expressed relatively unstable and lower repeatability during the same tests. Also, the working range (strength) and the recovery speed of the CEF were relatively worse than the CSRT. However, the CEF still shows the ability being an open circuit alarm, the breakpoint would occur every time when the load reach ~38.2 N.

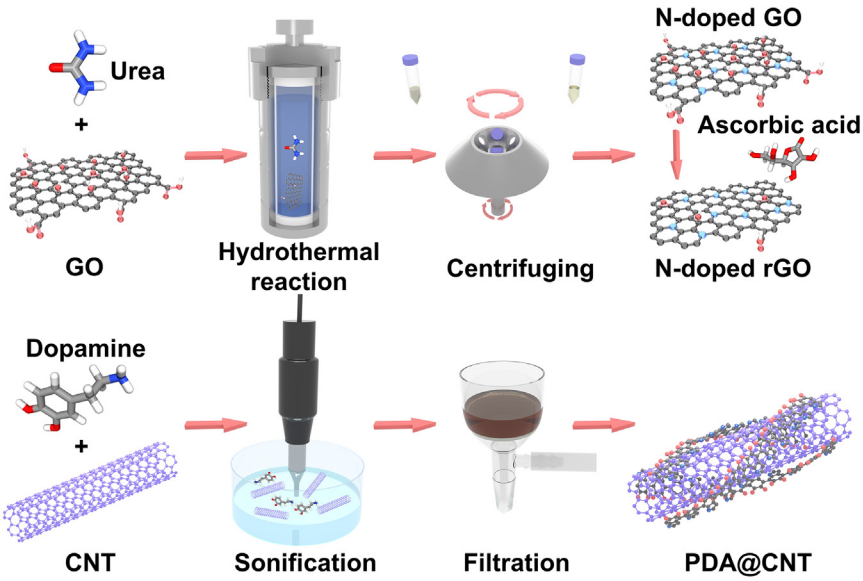

Figure 10. Schematic diagram of N-doped rGO and PDA@CNT

To improve the sensitivity of the CSRT to sense slightly force, it was shaped into different structures via the tailored fiber placement technique. The finite element analysis results confirmed that bending curves of the sensor structure could provide a pre-load to the sensor, then improve the ability to sense slight movement or simulate (the sensitivity of the three structures improved 4–9 times than straight filament); especially the one bending curve structure exhibits excellent sensitivity of slight movement/simulate, and the good response speed and repeatability. Moreover, it represents the capability of human bio-signal sensing, especially the cardiorespiratory signal. The sensor was tested under different respiration speeds, under each situation, it could capture and monitor reliable, stable, and precise breathing as well as cardiac signals. Finally, the sensor was fixed on a vest, it still exhibited high sensitivity and accuracy for bio-signal sensing even without the help of any elastic band. The above results demonstrate that the CSRT sensor would be an essential step toward realizing the bio-signal sensing of wearable e-textile for next-generation health care devices. Moreover, once the CSRT is prepared for mass production, the continuous CSRT can be cut into shorter pieces with different lengths as required, thus providing tailor-made choices for potential customers.

Limitations of the study

In this article, we fabricated the conductive silicon rubber tube by filling PDA@CNT and N-doped rGO matrix inside the silicon rubber tube. It shows excellent durability, stability, and sensitivity. In addition, its sensitivity can be adjusted by bending the conductive silicon rubber tube to different angles. Due to the silicon rubber tube chose in this article having a relatively higher rigidity lower extendibility, the conductive silicon rubber tube did not exhibit the sensibility of strain. It is worth noting that choosing an elastic material with higher softness and better ductility as the substrate will result in a decrease in the recoverability of the final sensor as well as the occurrence of deepened hysteresis, which has been observed in the results of CEF. Moreover, the filling conductive materials are dried PDA@CNT and N-doped rGO powders, it might lead to an open-circuit or unstable signal output during the tensile test.

STAR★METHODS

Detailed methods are provided in the online version of this paper and include the following:

- KEY RESOURCES TABLE
- RESOURCE AVAILABILITY
  - Lead contact
  - Materials availability
  - Data and code availability

- METHOD DETAILS
  - Preparation of conductive silicon rubber tube
  - Characterization
  - Sensing performance of the CSRT and CEF
  - Modelling and pre-load analysis in ABAQUS
  - Fabrication of the embroidered sensor and bio-signal sensing

SUPPLEMENTAL INFORMATION

Supplemental information can be found online at https://doi.org/10.1016/j.isci.2023.106403.

ACKNOWLEDGMENTS

SA and NK are supported by funding from UKRI Research England The Expanding Excellence in England (E3) grant. MRI is supported by the UWE partnership PhD award. This work is also supported by the National Natural Science Foundation of China (Grant Number 52202024).

AUTHOR CONTRIBUTIONS

Sirui Tan: Investigation, Data Curation, Formal analysis, Writing - Original Draft.

Shaila Afroj: Validation, Funding acquisition, Writing - Review & Editing.

Daiqi Li: Validation, Funding acquisition.

Md Rashedul Islam: Writing - Review & Editing.

Jihong Wu: Supervision, Resources.

Guangming Cai: Supervision, Resources.

Nazmul Karim: Project administration, Funding acquisition, Writing - Review & Editing.

Zhong Zhao: Conceptualization, Methodology, Visualization, Writing - Review & Editing.

DECLARATION OF INTERESTS

The authors declare no competing Interests.

Received: November 15, 2022
Revised: February 27, 2023
Accepted: March 10, 2023
Published: March 15, 2023

REFERENCES

1. Libanori, A., Chen, G., Zhao, X., Zhou, Y., and Chen, J. (2022). Smart textiles for personalized healthcare. Nat. Electron. *5*, 142–156. https://doi.org/10.1038/s41928-022-00723-z.

2. Islam, M.R., Afroj, S., Beach, C., Islam, M.H., Parraman, C., Abdelkader, A., Casson, A.J., Novoselov, K.S., and Karim, N. (2022). Fully printed and multifunctional graphene-based wearable e-textiles for personalized healthcare applications. iScience *25*, 103945. https://doi.org/10.1016/j.isci.2022.103945.

3. Kong, W.-W., Zhou, C.-G., Dai, K., Jia, L.-C., Yan, D.-X., and Li, Z.-M. (2021). Highly stretchable and durable fibrous strain sensor with growth ring-like spiral structure for wearable electronics. Compos. B Eng. *225*, 109275. https://doi.org/10.1016/j.compositesb.2021.109275.

4. Karim, N., Afroj, S., Tan, S., He, P., Fernando, A., Carr, C., and Novoselov, K.S. (2017). Scalable production of graphene-based wearable E-textiles. ACS Nano *11*, 12266–12275. https://doi.org/10.1021/acsnano.7b05921.

5. Afroj, S., Karim, N., Wang, Z., Tan, S., He, P., Holwill, M., Ghazaryan, D., Fernando, A., and Novoselov, K.S. (2019). Engineering graphene flakes for wearable textile sensors via highly scalable and ultrafast yarn dyeing technique. ACS Nano *13*, 3847–3857. https://doi.org/10.1021/acsnano.9b00319.

6. Eskandarian, L., Lam, E., Rupnow, C., Meghrazi, M.A., and Naguib, H.E. (2020). Robust and multifunctional conductive yarns for biomedical textile computing. ACS Appl. Electron. Mater. *2*, 1554–1566. https://doi.org/10.1021/acsaelm.0c00171.

7. Fan, W., He, Q., Meng, K., Tan, X., Zhou, Z., Zhang, G., Yang, J., and Wang, Z.L. (2020). Machine-knitted washable sensor array textile for precise epidermal physiological signal monitoring. Sci. Adv. *6*, eaay2840.

8. Ke, Y., Jia, K., Zhong, W., Ming, X., Jiang, H., Chen, J., Ding, X., Li, M., Lu, Z., and Wang, D. (2022). Wide-range sensitive all-textile piezoresistive sensors assembled with biomimetic core-shell yarn via facile

embroidery integration. Chem. Eng. J. *435*, 135003. https://doi.org/10.1016/j.cej.2022.135003.

9. Tan, S., Islam, M.R., Li, H., Fernando, A., Afroj, S., and Karim, N. (2022). Highly scalable, sensitive and ultraflexible graphene-based wearable E-textiles sensor for bio-signal detection. Advanced Sensor Research *1*, 2200010. https://doi.org/10.1002/adsr.202200010.

10. Rajan, G., Morgan, J.J., Murphy, C., Torres Alonso, E., Wade, J., Ott, A.K., Russo, S., Alves, H., Craciun, M.F., and Neves, A.I.S. (2020). Low operating voltage carbon-graphene hybrid E-textile for temperature sensing. ACS Appl. Mater. Interfaces *12*, 29861–29867. https://doi.org/10.1021/acsami.0c08397.

11. Rothmaier, M., Selm, B., Spichtig, S., Haensse, D., and Wolf, M. (2008). Photonic textiles for pulse oximetry. Opt Express *16*, 12973–12986. https://doi.org/10.1364/oe.16.012973.

12. Tang, J., Wu, Y., Ma, S., Yan, T., and Pan, Z. (2022). Flexible strain sensor based on CNT/TPU composite nanofiber yarn for smart sports bandage. Compos. B Eng. *232*, 109605. https://doi.org/10.1016/j.compositesb.2021.109605.

13. Afroj, S., Islam, M.H., and Karim, N. (2021). Multifunctional graphene-based wearable E-textiles. Proceedings *68*, 11. https://doi.org/10.3390/proceedings2021068011.

14. Dulal, M., Afroj, S., Ahn, J., Cho, Y., Carr, C., Kim, I.-D., and Karim, N. (2022). Toward sustainable wearable electronic textiles. ACS Nano *16*, 19755–19788. https://doi.org/10.1021/acsnano.2c07723.

15. Maity, D., and Kumar, R.T.R. (2018). Polyaniline anchored MWCNTs on fabric for high performance wearable ammonia sensor. ACS Sens. *3*, 1822–1830. https://doi.org/10.1021/acssensors.8b00589.

16. Chen, S., Peng, S., Sun, W., Gu, G., Zhang, Q., and Guo, X. (2019). Scalable processing ultrathin polymer dielectric films with a generic solution based approach for wearable soft electronics. Adv. Mater. Technol. *4*, 1800681. https://doi.org/10.1002/admt.201800681.

17. Zahid, M., Zych, A., Dussoni, S., Spallanzani, G., Donno, R., Maggiali, M., and Athanassiou, A. (2021). Wearable and self-healable textile-based strain sensors to monitor human muscular activities. Compos. B Eng. *220*, 108969. https://doi.org/10.1016/j.compositesb.2021.108969.

18. Pham, V.P., Jang, H.S., Whang, D., and Choi, J.Y. (2017). Direct growth of graphene on rigid and flexible substrates: progress, applications, and challenges. Chem. Soc. Rev. *46*, 6276–6300. https://doi.org/10.1039/c7cs00224f.

19. Windmiller, J.R., and Wang, J. (2013). Wearable electrochemical sensors and biosensors: a review. Electroanalysis *25*, 29–46. https://doi.org/10.1002/elan.201200349.

20. Afroj, S., Britnell, L., Hasan, T., Andreeva, D.V., Novoselov, K.S., and Karim, N. (2021). Graphene-based technologies for tackling COVID-19 and future pandemics. Adv. Funct. Mater. *31*, 2107407. https://doi.org/10.1002/adfm.202107407.

21. Wang, D., Choi, D., Li, J., Yang, Z., Nie, Z., Kou, R., Hu, D., Wang, C., Saraf, L.V., Zhang, J., et al. (2009). Self-Assembled TiO2–graphene hybrid nanostructures for enhanced Li-ion insertion. ACS Nano *3*, 907–914.

22. Islam, M.R., Afroj, S., Novoselov, K.S., and Karim, N. (2022). Smart electronic textile-based wearable supercapacitors. Adv. Sci. *9*, 2203856. https://doi.org/10.1002/advs.202203856.

23. Maiti, S., Islam, M.R., Uddin, M.A., Afroj, S., Eichhorn, S.J., and Karim, N. (2022). Sustainable fiber-reinforced composites: a review. Advanced Sustainable Systems *6*, 2200258. https://doi.org/10.1002/adsu.202200258.

24. Li, Z., Guo, Q., Li, Z., Fan, G., Xiong, D.B., Su, Y., Zhang, J., and Zhang, D. (2015). Enhanced mechanical properties of graphene reduced graphene oxide/aluminum composites with a bioinspired nanolaminated structure. Nano Lett. *15*, 8077–8083. https://doi.org/10.1021/acs.nanolett.5b03492.

25. Karim, N., Sarker, F., Afroj, S., Zhang, M., Potluri, P., and Novoselov, K.S. (2021). Sustainable and multifunctional composites of graphene-based natural jute fibers. Adv. Sustain. Syst. *5*, 2000228. https://doi.org/10.1002/adsu.202000228.

26. Islam, M.H., Islam, M.R., Dulal, M., Afroj, S., and Karim, N. (2022). The effect of surface treatments and graphene-based modifications on mechanical properties of natural jute fiber composites: a review. iScience *25*, 103597. https://doi.org/10.1016/j.isci.2021.103597.

27. Fan, W., Chu, R., Wang, C., Song, H., Ding, Y., Li, X., Jiang, M., Li, Q., Liu, L., and He, A. (2021). Synthesis and characteristic of the ternary composite electrode material PTCDA/CNT@MPC and its electrochemical performance in sodium ion battery. Compos. B Eng. *226*, 109329. https://doi.org/10.1016/j.compositesb.2021.109329.

28. Islam, M.H., Afroj, S., Uddin, M.A., Andreeva, D.V., Novoselov, K.S., and Karim, N. (2022). Graphene and CNT-based smart fiber-reinforced composites: a review. Adv. Funct. Mater. *32*, 2205723. https://doi.org/10.1002/adfm.202205723.

29. Zhou, H., Lai, J., Zheng, B., Jin, X., Zhao, G., Liu, H., Chen, W., Ma, A., Li, X., and Wu, Y. (2021). From glutinous-rice-inspired adhesive organohydrogels to flexible electronic devices toward wearable sensing, power supply, and energy storage. Adv. Funct. Mater. *32*, 2108423. https://doi.org/10.1002/adfm.202108423.

30. Veeralingam, S., and Badhulika, S. (2021). Bi2S3/PVDF/Ppy-Based freestanding, wearable, transient nanomembrane for ultrasensitive pressure, strain, and temperature sensing. ACS Appl. Bio Mater. *4*, 14–23. https://doi.org/10.1021/acsabm.0c01399.

31. Dai, Z., Ding, S., Lei, M., Li, S., Xu, Y., Zhou, Y., and Zhou, B. (2021). A superhydrophobic and anti-corrosion strain sensor for robust underwater applications. J. Mater. Chem. *9*, 15282–15293. https://doi.org/10.1039/d1ta04259a.

32. Zeng, Z., Hao, B., Li, D., Cheng, D., Cai, G., and Wang, X. (2021). Large-scale production of weavable, dyeable and durable spandex/CNT/cotton core-sheath yarn for wearable strain sensors. Compos. Appl. Sci. Manuf. *149*, 106520. https://doi.org/10.1016/j.compositesa.2021.106520.

33. Afroj, S., Tan, S., Abdelkader, A.M., Novoselov, K.S., and Karim, N. (2020). Highly conductive, scalable, and machine washable graphene-based E-textiles for multifunctional wearable electronic applications. Adv. Funct. Mater. *30*, 2000293. https://doi.org/10.1002/adfm.202000293.

34. Kim, G.M., Choi, W.Y., Park, J.H., Jeong, S.J., Hong, J.-E., Jung, W., and Lee, J.W. (2020). Electrically conductive oxidation-resistant boron-coated carbon nanotubes derived from atmospheric CO_2 for use at high temperature. ACS Appl. Nano Mater. *3*, 8592–8597. https://doi.org/10.1021/acsanm.0c01909.

35. Joh, H., Lee, S.W., Seong, M., Lee, W.S., and Oh, S.J. (2017). Engineering the charge transport of Ag nanocrystals for highly accurate, wearable temperature sensors through all-solution processes. Small *13*, 1700247. https://doi.org/10.1002/smll.201700247.

36. Zhou, X., Zhu, L., Fan, L., Deng, H., and Fu, Q. (2018). Fabrication of highly stretchable, washable, wearable, water-repellent strain sensors with multi-stimuli sensing ability. ACS Appl. Mater. Interfaces *10*, 31655–31663. https://doi.org/10.1021/acsami.8b11766.

37. Gao, H., Liu, H., Song, C., and Hu, G. (2019). Infusion of graphene in natural rubber matrix to prepare conductive rubber by ultrasound-assisted supercritical CO_2 method. Chem. Eng. J. *368*, 1013–1021. https://doi.org/10.1016/j.cej.2019.03.026.

38. Cheng, X., Zhang, F., Bo, R., Shen, Z., Pang, W., Jin, T., Song, H., Xue, Z., and Zhang, Y. (2021). An anti-fatigue design strategy for 3D ribbon-shaped flexible electronics. Adv. Mater. *33*, e2102684. https://doi.org/10.1002/adma.202102684.

39. Zhang, S., Zhao, Y., Du, X., Chu, Y., Zhang, S., and Huang, J. (2019). Gas sensors based on nano/microstructured organic field-effect transistors. Small *15*, 1805196.

40. Lin, L., Li, J., Yuan, Q., Li, Q., Zhang, J., Sun, L., Rui, D., Chen, Z., Jia, K., Wang, M., et al. (2019). Nitrogen cluster doping for high-mobility/conductivity graphene films with millimeter-sized domains. Sci. Adv. *5*, eaaw8337.

41. Zou, R., Liu, F., Hu, N., Ning, H., Gong, Y., Wang, S., Huang, K., Jiang, X., Xu, C., Fu, S.,

et al. (2020). Graphene/graphitized polydopamine/carbon nanotube all-carbon ternary composite films with improved mechanical properties and through-plane thermal conductivity. ACS Appl. Mater. Interfaces *12*, 57391–57400. https://doi.org/10.1021/acsami.0c18373.

42. Davoodi, E., Montazerian, H., Haghniaz, R., Rashidi, A., Ahadian, S., Sheikhi, A., Chen, J., Khademhosseini, A., Milani, A.S., Hoorfar, M., and Toyserkani, E. (2020). 3D-Printed ultra-robust surface-doped porous silicone sensors for wearable biomonitoring. ACS Nano *14*, 1520–1532. https://doi.org/10.1021/acsnano.9b06283.

43. Kalaoglu-Altan, O.I., Kayaoglu, B.K., and Trabzon, L. (2022). Improving thermal conductivities of textile materials by nanohybrid approaches. iScience *25*, 103825. https://doi.org/10.1016/j.isci.2022.103825.

44. Wang, Z., Chen, Y., Yao, M., Dong, J., Zhang, Q., Zhang, L., and Zhao, X. (2020). Facile fabrication of flexible rGO/MXene hybrid fiber-like electrode with high volumetric capacitance. J. Power Sources *448*, 227398. https://doi.org/10.1016/j.jpowsour.2019.227398.

45. Wang, Y., Zhu, L., Mei, D., and Zhu, W. (2019). A highly flexible tactile sensor with an interlocked truncated sawtooth structure based on stretchable graphene/silver/silicone rubber composites. J. Mater. Chem. C *7*, 8669–8679. https://doi.org/10.1039/c9tc02356a.

46. Dong, K., Wang, Y.C., Deng, J., Dai, Y., Zhang, S.L., Zou, H., Gu, B., Sun, B., and Wang, Z.L. (2017). A highly stretchable and washable all-yarn-based self-charging knitting power textile composed of fiber triboelectric nanogenerators and supercapacitors. ACS Nano *11*, 9490–9499. https://doi.org/10.1021/acsnano.7b05317.

47. Hu, Q., Bai, X., Zhang, C., Zeng, X., Huang, Z., Li, J., Li, J., and Zhang, Y. (2022). Oriented BN/Silicone rubber composite thermal interface materials with high out-of-plane thermal conductivity and flexibility. Compos. Appl. Sci. Manuf. *152*, 106681. https://doi.org/10.1016/j.compositesa.2021.106681.

48. Montazerian, H., Rashidi, A., Dalili, A., Najjaran, H., Milani, A.S., and Hoorfar, M. (2019). Graphene-coated spandex sensors embedded into silicone sheath for composites health monitoring and wearable applications. Small *15*, e1804991. https://doi.org/10.1002/smll.201804991.

49. Li, J., Zou, Y., Jin, L., Xu, F., Sun, L., and Xiang, C. (2022). Polydopamine-assisted $NiMoO_4$ nanorods anchored on graphene as an electrode material for supercapacitor applications. J. Energy Storage *50*, 104639. https://doi.org/10.1016/j.est.2022.104639.

50. Qin, Y., Yuan, J., Li, J., Chen, D., Kong, Y., Chu, F., Tao, Y., and Liu, M. (2015). Crosslinking graphene oxide into robust 3D porous N-doped graphene. Adv. Mater. *27*, 5171–5175. https://doi.org/10.1002/adma.201501735.

51. Zhai, J., Zhang, Y., Cui, C., Li, A., Wang, W., Guo, R., Qin, W., Ren, E., Xiao, H., and Zhou, M. (2021). Flexible waterborne polyurethane/cellulose nanocrystal composite aerogels by integrating graphene and carbon nanotubes for a highly sensitive pressure sensor. ACS Sustainable Chem. Eng. *9*, 14029–14039. https://doi.org/10.1021/acssuschemeng.1c03068.

52. Song, D., Zeng, M.-J., Min, P., Jia, X.-Q., Gao, F.-L., Yu, Z.-Z., and Li, X. (2023). Electrically conductive and highly compressible anisotropic MXene-wood sponges for multifunctional and integrated wearable devices. J. Mater. Sci. Technol. *144*, 102–110.

53. Cheng, H., Zhang, N., Yin, Y., and Wang, C. (2021). A high–performance flexible piezoresistive pressure sensor features an integrated design of conductive fabric electrode and polyurethane sponge. Macromol. Mater. Eng. *306*, 2100263.

54. Wei, X., Cao, X., Wang, Y., Zheng, G., Dai, K., Liu, C., and Shen, C. (2017). Conductive herringbone structure carbon nanotube/thermoplastic polyurethane porous foam tuned by epoxy for high performance flexible piezoresistive sensor. Compos. Sci. Technol. *149*, 166–177.

55. Lv, B., Chen, X., and Liu, C. (2020). A highly sensitive piezoresistive pressure sensor based on graphene oxide/polypyrrole@polyurethane sponge. Sensors *20*, 1219.

56. Ma, Z., Wei, A., Ma, J., Shao, L., Jiang, H., Dong, D., Ji, Z., Wang, Q., and Kang, S. (2018). Lightweight, compressible and electrically conductive polyurethane sponges coated with synergistic multiwalled carbon nanotubes and graphene for piezoresistive sensors. Nanoscale *10*, 7116–7126.

57. Mu, Y., Wang, L., Zhang, R., Pashameah, R.A., Alzahrani, E., Li, Z., Alanazi, A.K., Algadi, H., Huang, M., Guo, Z., et al. (2023). Rapid and facile fabrication of hierarchically porous graphene aerogel for oil-water separation and piezoresistive sensing applications. Appl. Surf. Sci. *613*, 155982.

58. Xu, S., Li, X., Sui, G., Du, R., Zhang, Q., and Fu, Q. (2020). Plasma modification of PU foam for piezoresistive sensor with high sensitivity, mechanical properties and long-term stability. Chem. Eng. J. *381*, 122666.

59. Iglio, R., Mariani, S., Robbiano, V., Strambini, L., and Barillaro, G. (2018). Flexible polydimethylsiloxane foams decorated with multiwalled carbon nanotubes enable unprecedented detection of ultralow strain and pressure coupled with a large working range. ACS Appl. Mater. Interfaces *10*, 13877–13885.

60. Zang, Y., Zhang, F., Di, C.-a., and Zhu, D. (2015). Advances of flexible pressure sensors toward artificial intelligence and health care applications. Mater. Horiz. *2*, 140–156. https://doi.org/10.1039/c4mh00147h.

61. Li, X., Li, S., Wu, M., Weng, Z., Ren, Q., Xiao, P., Wang, L., and Zheng, W. (2023). Multifunctional polyether block amides/carbon nanostructures piezoresistive foams with largely linear range, enhanced and humidity-regulated microwave shielding. Chem. Eng. J. *455*, 140860.

62. Huang, L., Chen, J., Xu, Y., Hu, D., Cui, X., Shi, D., and Zhu, Y. (2021). Three-dimensional light-weight piezoresistive sensors based on conductive polyurethane sponges coated with hybrid CNT/CB nanoparticles. Appl. Surf. Sci. *548*, 149268.

63. Karim, N., Afroj, S., Leech, D., and Abdelkader, A.M. (2021). Flexible and wearable graphene-based E-textiles. In Oxide Electronics, pp. 21–49. https://doi.org/10.1002/9781119529538.ch2.

64. Karim, N., Afroj, S., Tan, S., Novoselov, K.S., and Yeates, S.G. (2019). All inkjet-printed graphene-silver composite ink on textiles for highly conductive wearable electronics applications. Sci. Rep. *9*, 8035. https://doi.org/10.1038/s41598-019-44420-y.

65. Yousaf, Z., Sajjad, S., Leghari, S.A.K., Noor, S., Kanwal, A., Bhatti, S.H., Mahmoud, K.H., and El-Bahy, Z.M. (2021). Influence of integrated nitrogen functionalities in nitrogen doped graphene modified WO3 functional visible photocatalyst. J. Environ. Chem. Eng. *9*, 106746. https://doi.org/10.1016/j.jece.2021.106746.

66. Marechal, L., Balland, P., Lindenroth, L., Petrou, F., Kontovounisios, C., and Bello, F. (2021). Toward a common framework and database of materials for soft robotics. Soft Robot. *8*, 284–297.

STAR★METHODS

KEY RESOURCES TABLE

REAGENT or RESOURCE	SOURCE	IDENTIFIER
Chemicals, peptides, and recombinant proteins		
Urea	Sinopharm (Shanghai, China)	Cat#10023218; CAS no. 57-13-6
Carbon nanotubes	Macklin Inc (Shanghai, China)	Cat#C805983; CAS no. 308068-56-6
Tris(hydroxymethyl)aminomethane	Meryer (Shanghai, China)	Cat#M26450; CAS no. 77-86-1
Dopamine hydrochloride	Aladdin (Shanghai, China)	Cat#D103111; CAS no. 62-31-7
Graphene oxide suspension	Macklin Inc (Shanghai, China)	Cat#S926159; CAS no. 7782-42-5
Ecoflex 00–20	Smooth-On Inc (Macungie, USA)	SDS No. 823A

RESOURCE AVAILABILITY

Lead contact

Further information and requests for resources and reagents should be directed to and will be fulfilled by the lead contact, Zhong Zhao (zzhao@wtu.edu.cn).

Materials availability

This study did not generate new unique reagents.

Data and code availability

The published article includes all data generated or analyzed during this study.

METHOD DETAILS

Preparation of conductive silicon rubber tube

Urea was employed as the nitrogen source to dope rGO following a modified process reported by Yousaf et al.[65] As demonstrated in Figure 10, 3 g urea was dissolved in 50 mL graphene oxide (GO) suspension (2 mg/mL) under sonification for 30 min. Nitrogen doping of GO was carried out by transferring the suspension into an autoclave and subjecting it to hydrothermal reaction at 180 °C for 5 h. After the hydrothermal reaction, the N-doped GO in the suspension was collected via centrifugation and then thoroughly rinsed with deionized water. Finally, N-doped GO was dispersed in L-ascorbic acid solution and reduced to N-doped rGO by heating the dispersion at 85 °C for 2 h.

2 g dopamine hydrochloride was dissolved in 1 L deionized water. The pH of the dopamine solution was then buffered to ~8.5 by dissolving 1.2 g Tris(hydroxymethyl) aminomethane in it. 1 g CNTs was subsequently dispersed into the dopamine solution. Dopamine formed a polydopamine (PDA) layer on the CNTs by dispersing CNTs into the dopamine hydrochloride solution under sonication for 30 min. The PDA coated CNTs (PDA@CNT) were collected via vacuum filtration. Finally, the collected solid was rinsed with deionized water to remove the excess chemicals and dried in dark at room temperature.

0.2 g N-doped rGO and 1 g PDA@CNT were added into 20 mL ethanol. The mixture was then subjected to vigorous sonication to form a suspension of the two materials. Finally, a paste was obtained by reducing the volume of the suspension to 10 mL through the evaporation of ethanol, which was realized by heating the suspension at 60 °C for 10 min in an oven. The paste was employed as the filling material and loaded into the pore of the silicon rubber tube *via* vacuum filling. When this vacuum filling process was duplicated in the industrial level, the conductive paste can be loaded into longer silicon rubber tube to manufact continuous CSRT efficiently. A relatively large inner diameter of the tube will result in the adhesion of the powder only onto the inner wall, while a relatively small inner diameter will cause the insufficient loading amount of the powder. Therefore, to ensure sufficient amount of powder loaded into the tube and balance the flexibility of the tube, a silicon rubber tube with the outer and inner diameters of 2 and 1 mm were used as the container. Two stainless-steel rods with the diameter of 1.5 mm and the conductivity of 2.83 S/m were

inserted 5 mm into the two ends of CSRT. The seams between the silicon rubber tube and the stainless-steel rods were sealed with Ecoflex to avoid the leakage of the conductive powder.

To reveal the influence of the structure of the silicon rubber tube on the performance of the sensor, a similar filament with the matrix of Ecoflex was set as control and tested along with the CSRT filament during the compression, bending and respiratory tests. Specifically, 1 g mixed powder comprised of the N-doped rGO and PDA@CNT (w/w = 1: 5) was dispersed into 10 mL A and B components of Ecoflex, respectively. The two dispersions were then mixed together *via* manual stirring and loaded into a syringe which was then pre-heated to 70 °C. The Ecoflex elastomer was then extruded from the syringe and immersed into a hot water bath (70 °C) for curing. A piece of CEF featuring a diameter of 2 mm and even distribution of the mixed powder in it was obtained after retrieving the cured Ecoflex sample from the water bath and drying it at 50 °C. The prominent flexibility of CSRT (Figure 3A) ensures the wearable characteristic of the tube-shaped composite while doping rGO with nitrogen is beneficial for the further improvement of its conductivity (Figure S5), making CSRT the candidate for the sensor with subtle action sensing ability.

Characterization

The PDA@CNT was scanned by a Talos F200x TEM (FEI, USA) to examine the coverage of PDA on the CNTs. To further reveal the composition of PDA@CNT, mapping of the elements was conducted using a Super-X EDS analyzer equipped with the TEM. The morphology of the filling material was characterized *via* a GeminiSEM 300 SEM (ZEISS, Germany), while its composition was analyzed by a ESCALAB Xi+ XPS analyzer (Thermo Fisher Scientific, USA) and a D8 Advance X-ray diffractor (Bruker, Germany).

Sensing performance of the CSRT and CEF

The electro-mechanical properties of the prepared two sensors were carried out using a 507A computerized tensile testing machine (DongRi instrument Co., Ltd., China). Specifically, the CSRT or CEF were tightly compressed by the two compression boards of a 507A computerized tensile testing machine. The sensor was then compressed by keeping the lower board stationary and moving the upper board downwards at a speed of 2 mm/min (Figure S8). 0–40 N compression force was applied on the sensors for the single and stepped cyclic tests.

The sensitivity (S) of a piezoresistive sensor is an essential parameter for the assessment of the device performance and was characterized using the following equation:

$$S = \frac{\Delta R}{R_0} \times 100\% = \frac{R - R_0}{R_0} \times 100\%$$

where ΔR denote the resistance change before and after load applied, R and R_0 denotes the loaded and unloaded samples' resistances, respectively. Various cord lengths were used during the bending test to measure the changes in resistance of CSRT and CEF sensors (40 mm). The cord length of the sensor was controlled by adjusting the distance between the two holders of the tensile machine. A certain length of the CSRT and CEF sensor (40 mm) were placed under an elastic band on the lower chest location of two participants for the respiratory and heart beat signal capturing. The changes in the resistance of the sensor during the mechanical tests on the tensile machine, bending tests on the machine, heart beat and respiration monitoring were measured and recorded *via* a half-bridge circuit built in a NI-9219 data acquisition card (National instrument, USA). Approval of the publication of cardiorespiratory data has been granted by both the two participants.

Modelling and pre-load analysis in ABAQUS

A cylinder model (Figure S6) featuring a tube and a finer cylinder whose diameter fits exactly the inner diameter of the tube was established in ABAQUS. The finer cylinder was mounted in the center of the tube to simulate the core-sheath structure of the silicon rubber tube filled with conductive powder. The finer cylinder was shorter than the tube while their difference in length was compensated by two shorter rods whose one end was in close contact with the end faces of the finer cylinder. The two rods stick out from each end of the tube and act as the electrodes of the sensor. To simulate the intrinsic mechanical properties of silicon rubber, powder and stainless steel, the materials of the tube, the finer cylinder and the rods were set as isotropic hyper-elastic solid with the C10 value of 0.02264 and the D1 value of 0,[66] isotropic elastic solid with the Young's modulus of 0.05 and Poisson's ratio of 0.4, and uniform solid with the mass density of 7.8×10^{-9}, respectively. The linear model was then bended into a "U" shape and the strain inside the

tube and the equivalent conductive powder unit was calculated using ABAQUS/Explicit. The damping approximation quasi-static analysis was employed to eliminate the vibration during the bending process.

Fabrication of the embroidered sensor and bio-signal sensing

The CSRT was fixed on the cotton woven fabric as different structures by using the creative 1.5 Cherry computerized embroidery machine (PFAFF, Germany). Tailored fiber placement (TFP) presser foot was used to place the CSRT yarn on the substrate fabric. The TFP structures were subjected to compression tests under the same conditions specified in (Figure 2). The structure with relatively better performance was selected and used to capture bio-signals. Sensor was mounted on the below chest and chest location to measure the breath and heartbeat signals respectively, and it was placed under the wrist to detect the pulse signals. Finally, the sensor was fixed on a Lycra vest on the chest location to measure the cardiorespiratory signals without the elastic band. The changes in resistance of the embroidered sensor during the mechanical tests and the bio-signal sensing on the human body were measured and recorded via the half-bridge circuit provided by the NI-9219 data acquisition card.